GEOPHYSICS, VOL. 68, NO. 4 (JULY-AUGUST 2003); P. 1173–1181, 8 FIGS., 2 TABLES.
10.1190/1.1598110

Incorporating mechanisms of fluid pressure relaxation into inclusion-based models of elastic wave velocities

S. Richard Taylor* and Rosemary J. Knight‡

ABSTRACT

Our new method incorporates fluid pressure communication into inclusion-based models of elastic wave velocities in porous rocks by defining effective elastic moduli for fluid-filled inclusions. We illustrate this approach with two models: (1) flow between nearest-neighbor pairs of inclusions and (2) flow through a network of inclusions that communicates fluid pressure throughout a rock sample. In both models, we assume that pore pressure gradients induce laminar flow through narrow ducts, and we give expressions for the effective bulk moduli of inclusions. We compute P-wave velocities and attenuation in a model sandstone and illustrate that the dependence on frequency and water-saturation agrees qualitatively with laboratory data. We consider levels of water saturation from 0 to 100% and all wavelengths much larger than the scale of material heterogeneity, obtaining near-exact agreement with Gassmann theory at low frequencies and exact agreement with inclusion-based models at high frequencies.

INTRODUCTION

Inclusion-based effective medium theory (IBEMT) models the elastic behavior of heterogeneous systems. In the standard formulation, the system is represented by hydraulically-isolated inclusions in a homogeneous background (e.g., Kuster and Toksöz, 1974; Berryman, 1980a, b; le Ravalec et al., 1996). With a lack of hydraulic communication between the inclusions, this model cannot account for coupling between elastic deformation and local fluid flow. As a result, the inclusion-based approach provides an accurate description of elastic wave velocities only for the unrelaxed or high-frequency case. By allowing for complete communication between the inclusions, the relaxed, low-frequency case can be modeled (e.g., Endres and Knight, 1997). What is needed, however, is a description of elastic behavior from the low frequencies of seismic data to the high frequencies of laboratory data. Understanding this dispersion is necessary for accurately interpreting P-wave velocities at any given frequency and to relate velocities measured at laboratory frequencies to those measured at seismic frequencies.

The dependence of velocity on frequency has been attributed to two different mechanisms: Biot dynamic poroelasticity (Biot, 1956a, b) and local flow (Jones, 1986; Murphy et al., 1986). Theoretical models using both mechanisms have been developed by Dutta and Odé (1979), Dvorkin and coworkers [Dvorkin and Nur, 1993; Dvorkin et al., 1994, and Endres (1998)]. These models and the complementary experimental observations indicate that local flow is the dominant mechanism for a wide range of rock types and in-situ conditions (Endres, 1998).

The local flow mechanism describes fluid pressure communication in a heterogeneous porous medium in response to an elastic wave. The initial magnitude of the fluid pressure induced by the wave will vary spatially due to heterogeneity of the elastic response. With sufficient time to respond, fluid flow equilibrates the fluid pressures. The pore fluid eventually "relaxes" and acts elastically as one single effective fluid phase. For a given length scale of heterogeneity, a characteristic time τ corresponds with the relaxation process (le Ravalec et al., 1996), thereby defining a characteristic frequency $\omega_0 = 1/\tau$. The elastic response is described as relaxed if $T \gg \tau$ and unrelaxed if $T \ll \tau$, where T represents the time-scale of elastic deformation. The wave frequency ω determines the available response time, hence the term "low frequency" refers to the relaxed case and "high frequency" refers to the unrelaxed case.

In the present study, we model dispersion due to local flow using inclusion-based effective medium theory. Although inclusion-based modeling requires idealized pore space geometries (e.g., spheres or ellipsoids), it does describe the fundamental processes of elastic wave velocities in porous rocks (i.e., the elastic deformation of a solid containing fluid-filled voids). If there is no hydraulic communication between the

Manuscript received by the Editor August 2, 1999; revised manuscript received February 19, 2003.
*University of Waterloo, Department of Applied Mathematics, 200 University Avenue West, Waterloo, Ontario N2L 3G1, Canada. Email: sr2taylo@math.uwaterloo.ca.
‡Stanford University, Geophysics Department, Mitchell Building, Stanford, California 94305-2215. Email: rknight@pangea.stanford.edu.

inclusions, however, local flow will not be part of the elastic response and only the high-frequency, unrelaxed behavior can be modeled. In order to predict the variation in P-wave velocity with frequency, the inclusion-based approach must be modified for communication between the inclusions. This has been done by Endres and Knight (1997) and Xu (1998), allowing prediction in either the fully relaxed or fully unrelaxed limit. These models are limited and cannot estimate velocities at intermediate frequencies.

In this work, we use a standard inclusion-based model, but incorporate fluid pressure communication into the elastic response of the inclusions by defining a frequency-dependent effective bulk modulus for each inclusion. This approach has the advantage that once the effective moduli of the inclusions have been estimated, an IBEMT can be used to estimate the effective elastic moduli and wave velocities. We model P-wave velocity for the range of frequencies accessible to effective-medium theory: from the low- or zero-frequency limit, up to frequencies where the wavelength becomes comparable to the length scale of heterogeneity. We consider only media that are isotropic with respect to elastic wave propagation.

Our central objective is to illustrate that inclusion-based models can be modified to predict frequency-dependent behavior. The accuracy of our approach depends on the local flow model used to estimate the effective moduli of inclusions; we show two simple models to validate the approach. We first describe pore-scale fluid pressure communication using a model that considers only communication with the nearest neighboring pore via laminar (Poiseuille) flow. We then consider a more sophisticated model using a network of pores. Even with these simple models, we obtain results that agree exactly with previous unrelaxed (high-frequency) inclusion-based results (Berryman, 1980a, b), and that agree very well with low-frequency Gassmann theory (Gassmann, 1951).

A PORE-TO-PORE RELAXATION MODEL

Model development

To estimate the effective moduli of a fluid-filled inclusion requires a model of pore-scale fluid pressure communication. As a simple model of this communication, consider the case of two inclusions, each containing a single fluid phase, connected by a narrow duct. Fluid can flow through the duct in response to a pressure gradient. We model the volumetric flow rate q between the inclusions by

$$q = \gamma(p_1 - p_2), \tag{1}$$

where γ is the fluid conductivity (a function of the duct geometry and the fluid in the duct) and p_1, p_2 are the fluid pressures in the respective inclusions. Differences in the induced fluid pressures in the inclusions can be caused either by a difference in compliance of the fluids or by a difference in geometric compliance of the inclusions.

Assuming steady laminar (Poiseuille) flow and approximating the duct as a cylinder of radius r and length L containing a Newtonian fluid with viscosity η, γ is determined by (e.g., White, 1986, 305)

$$\gamma = \frac{\pi r^4}{8\eta L}. \tag{2}$$

For pressure relaxation between neighboring pores, the parameter L is the length scale of fluid pressure heterogeneity. For simplicity, we assume that the flow is not influenced by entrance and exit effects. We also assume that the duct radius is sufficiently small that flow develops fully on a time scale shorter than the wave period [Biot (1956b) derived the more general frequency-dependent version of equation (4) that treats the general case]. We further assume that only a single fluid phase occupies the duct. This is reasonable because of the affinity of wetting fluids for the smallest regions of the pore-space.

Using this local flow model, we derive in Appendix A the following expression for the effective bulk modulus κ_1^* for inclusion 1:

$$\kappa_1^* = \frac{\tilde{\kappa} + i\dfrac{\omega}{\omega_0}\kappa_1}{1 + i\dfrac{\omega}{\omega_0}} \tag{3}$$

where ω is angular frequency, ω_0 is the characteristic relaxation frequency, and κ_1 is the bulk modulus of the fluid in inclusion 1. Here $\tilde{\kappa}$ is

$$\tilde{\kappa} = \frac{P_1V_1 + P_2V_2}{P_1\left(\dfrac{V_1}{\kappa_1} + \dfrac{V_2}{\kappa_2}\right) + \dfrac{V_2}{\kappa_b}(P_2 - P_1)}, \tag{4}$$

where the quantities P_i [defined in Berryman (1980b)] account for the effects of inclusion geometries, the V_is are the inclusion volumes, κ_2 is the bulk modulus of the fluid in inclusion 2, and κ_b is the matrix bulk modulus. The relaxation frequency ω_0 is

$$\omega_0 = \frac{\gamma}{V_1V_2}\left[\frac{\kappa_1\kappa_2}{\kappa_b - \kappa_2 + P_2\kappa_2}\right] \times \left[\kappa_b\left(\frac{V_1}{\kappa_1} + \frac{V_2}{\kappa_2}\right) + V_2\left(\frac{P_2}{P_1} - 1\right)\right], \tag{5}$$

which defines the time-scale of relaxation, $\tau \sim 1/\omega_0$. Note that equation (3) describes the effective bulk modulus of the fluid component only. It does not include coupling with the stiffness of the dry (empty) pore, as the reader might have anticipated. Rather, applying an IBEMT [in which equation (3) models one of the medium's constituents] accounts for this geometrical effect. Although our model can account for a distribution of pore geometries, for simplicity we consider the case where all inclusions have the same geometry (i.e., $P_1 = P_2$). The reduced forms of equations (4)–(5) for this case are given in Appendix B.

Figure 1 shows a plot of the real and imaginary parts of κ_1^*/κ_1 versus ω/ω_0 for the particular case of spherical inclusions. We have set $\kappa_2/\kappa_1 = 0.1$ (i.e., inclusion 2 is filled with a fluid that is much more compressible than that in inclusion 1). As expected, in the high-frequency, unrelaxed limit, we have $\kappa_1^* = \kappa_1$ (i.e., the elastic response is unmodified by hydraulic communication). In the low-frequency limit where the fluid pressure is equal in the two inclusions, $\kappa_1^* = \tilde{\kappa}$. The behavior exhibited in Figure 1 is typical of viscous relaxation mechanisms (Mavko et al., 1998, 197), showing a distinct transition from low-frequency to high-frequency behavior, and a characteristic frequency ω_0 separating these regimes. Near ω_0, viscous dissipation (represented by the imaginary part of κ_1^*) has a characteristic peak, corresponding to a maximum (near 45°) of the phase angle by which the pressure in the pore leads the dilatation.

While it is conventionally assumed that fluids do not contribute to the shear stiffness of a porous composite, viscous

shear flow does contribute to elastic dissipation. Following Berryman (1980a, b), we account for this by using the expression $\mu^* = i\omega\eta$ for the effective shear modulus μ^* of an inclusion filled with fluid of viscosity η. This expression is based on fully developed shear flow under sinusoidal deformation. The fact that μ^* is purely imaginary reflects the purely viscous (i.e., inelastic) role of the fluid.

Using expression (3) for the effective moduli of two connected inclusions, we now consider a model porous medium containing a large number of inclusions. An important parameter in the description of fluid pressure communication is the interpore distance L which enters through γ. In a realistic porous medium represented by inclusions distributed randomly throughout a background matrix, L has a different value for every pair of inclusions. We therefore treat L as a random variable described by a probability distribution.

In Appendix C, we derive the probability density $P(R)$ of the distance R between centers of inclusions of any size or shape, distributed randomly with number density n (inclusions per unit volume). We obtain

$$P(R) = 4\pi n R^2 \exp\left(-\tfrac{4}{3}\pi n R^3\right). \qquad (6)$$

The parameter L is obtained by subtracting the size of the inclusions from R. Having determined the probability distribution of L, the distribution of effective bulk moduli of the inclusions follows directly from the relationship between L and κ_1^* given by equations (2)–(5). The distribution of effective moduli is incorporated into the IBEMT via the weights c_i in equations (29)–(30) of Berryman (1980b).

In our model, we assume that each inclusion is filled with either water or air, and that any water-filled inclusion communicates only with the nearest gas-filled inclusion. Thus, we used equation (6) with $n = n_g$, the number density of gas-filled pores, to compute the distances to gas-filled inclusions. [If the water saturation is S_w, then $n_g = (1 - S_w)n$.] The effect of saturation on the distance from a given water-filled inclusion to its nearest gas-filled neighbor is illustrated in Figure 2 by a graph of $P(R)$ for various values of n_g corresponding to different levels of saturation. This figure illustrates the expected behavior: that R, and hence L, becomes larger as water saturation is increased. It also illustrates that L becomes more broadly distributed with increasing saturation. This suggests that accounting for the random distribution of L becomes more important at higher levels of water saturation.

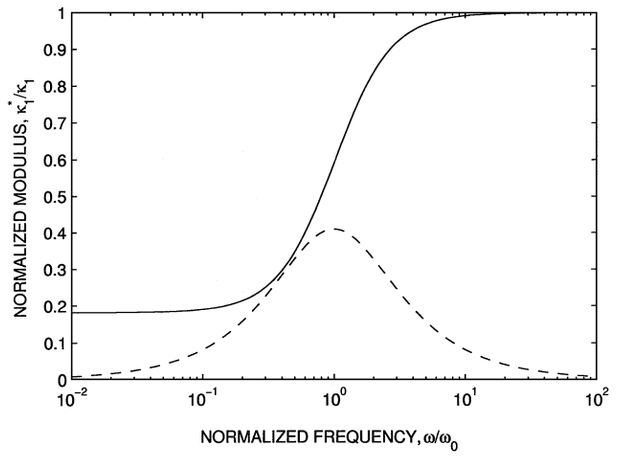

FIG. 1. Graphs of the real (solid) and imaginary (dashed) parts of the normalized effective bulk modulus κ_1^*/κ_1 versus ω/ω_0 as given by the pore-to-pore relaxation model [equation (3)], for hydraulic communication with an inclusion containing a very compressible fluid ($\kappa_2/\kappa_1 = 0.1$).

Modeling results and discussion

Using the model described above, we compute effective elastic moduli and wave velocities over a range of frequencies and levels of saturation for a "model sandstone." Our model sandstone is composed of water- and air-filled spherical inclusions in a solid quartz matrix. Data describing the physical properties of the constituent materials are given in Table 1; other parameters used in the model are given in Table 2. The elastic P-wave velocity and quality factor (v_p and Q_p^{-1}, respectively) for the model sandstone were computed using [Berryman, 1980b, equation (48)],

Table 1. Physical properties of the constituents of a model sandstone.

	Solid Grains (Quartz)[1]	Water[2]	Gas[2]
Bulk modulus, κ [Pa]	37×10^9	2.4×10^9	0.02×10^9
Shear modulus, μ [Pa]	44×10^9	0	0
density, ρ [kg/m^3]	2.65×10^3	1.0×10^3	100

[1]From Mavko et al. (1998, p. 307).
[2]From Dutta and Odé (1979).

Table 2. Parameters used to quantify the pore space and hydraulic properties of a model sandstone.

Parameter	Numerical Value
Porosity, ϕ	0.25
Inclusion radius, a	100 μm
Inclusion volume, $V = \frac{4}{3}\pi a^3$	0.0042 mm^3
Inclusion number density, $n = \phi/V$	36 mm^{-3}
Water viscosity, η	10^{-3} Pa · s
Duct radius, r	2.0 μm

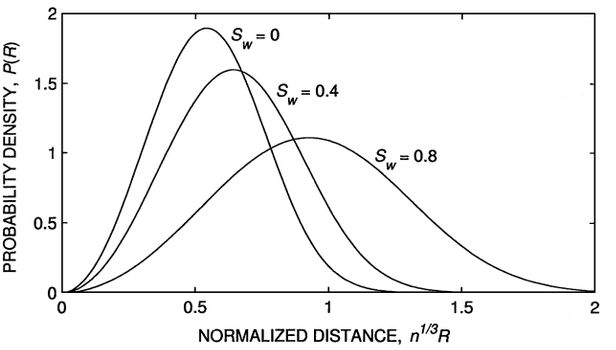

FIG. 2. Probability distribution [from equation (6)] of the distance, R, from the center of a given water-filled inclusion to the center of its nearest gas-filled neighbor, for various levels of water saturation, S_w.

$$\frac{1}{v_p}\left(1-\frac{i}{2}Q_p^{-1}\right)=\left(\frac{\rho}{\kappa_{\text{eff}}+\frac{4}{3}\mu_{\text{eff}}}\right)^{1/2}, \qquad (7)$$

where κ_{eff} and μ_{eff} are the computed (complex-valued) bulk and shear moduli of the composite, and ρ is the average density of the sample.

The resulting graphs of v_p versus S_w, at various frequencies are presented in Figure 3. The Gassmann curve was computed by first using the conventional inclusion-based model to compute the dry-frame bulk modulus κ_d and then applying Gassmann's equation,

$$\kappa_{\text{eff}}=\kappa_d+\frac{\alpha^2}{\frac{\phi}{\kappa_f}+\frac{\alpha-\phi}{\kappa_s}} \qquad (8)$$

to compute the effective bulk modulus κ_{eff} of the fluid-saturated sample. Here, κ_s is the bulk modulus of the solid mineral material (e.g., quartz), and $\alpha\equiv 1-\kappa_d/\kappa_s$ is typically termed the "poroelastic parameter." Because the pressure is equilibrated between the fluids, the bulk modulus κ_f of the effective fluid phase is given by the Reuss average,

$$\frac{1}{\kappa_f}=\frac{S_w}{\kappa_w}+\frac{1-S_w}{\kappa_g}, \qquad (9)$$

where κ_w and κ_g are the bulk moduli of the liquid and gas phases, respectively, and S_w is the liquid saturation. The conventional assumption of the Gassmann approach (that the shear modulus of the fluid-saturated composite is equal to dry-frame modulus) was used.

The high-frequency limit curve plotted in Figure 3 coincides with the result that would have been obtained if the IBEMT calculation had been performed with no fluid pressure communication between inclusions. As the frequency is decreased, allowing pore-to-pore relaxation of fluid pressure to occur, the composite becomes more compliant and the P-wave velocity correspondingly decreases. Note that in the low-frequency limit, where fluid pressures are equilibrated, the computed v_p versus S_w curve agrees closely with the low-frequency curve computed using Gassmann's equation. The cause of the discrepancy is that in the Gassmann formulation the fluid pressure is equilibrated throughout the pore space, whereas in the present model it is equilibrated only between pairs of inclusions (so that fluid pressures can be more relaxed in the low-frequency limit than would otherwise be possible). The velocity is frequency independent at 0 and 100% saturation because the pore fluid is homogeneous and therefore no pressure gradients arise that would cause flow. We present in Figure 4 the same data plotted in Figure 3, but as P-wave velocity vs. frequency.

The graph of Q_p^{-1} versus S_w resulting from the same simulation is presented in Figure 5; curves are plotted for three different frequencies between the high- and low-frequency limits. The qualitative features of each curve are similar, with a loss peak that occurs at a higher saturation as the wave frequency

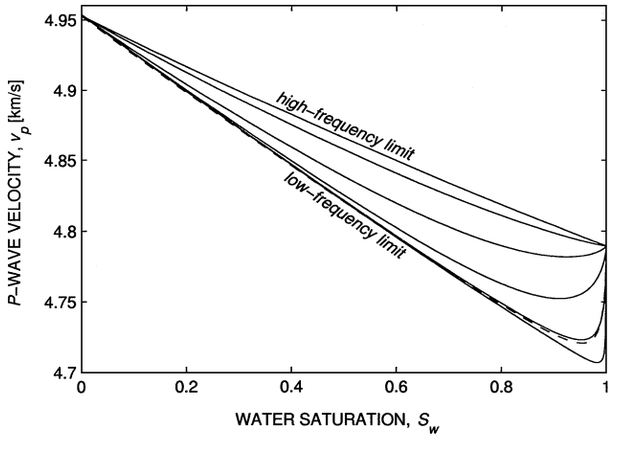

FIG. 3. Computed P-wave velocity, v_p, versus water saturation, S_w, for a model sandstone, as given by the pore-to-pore relaxation model. The solid curves correspond to each of the wave frequencies $10^{2.5}$, 10^3, $10^{3.5}$, 10^4, $10^{4.5}$, and 10^5 Hz. For comparison, the velocities predicted by Gassmann's equation are plotted as the dashed curve.

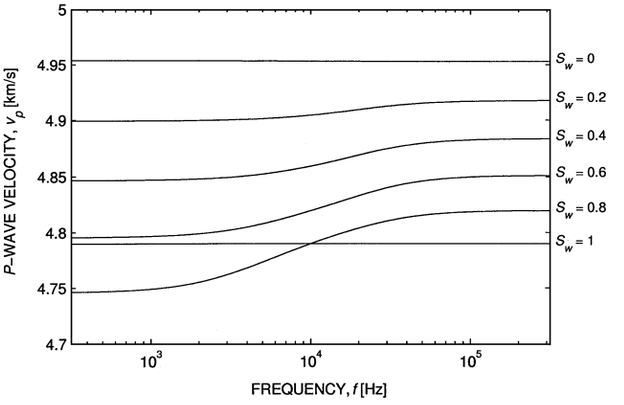

FIG. 4. Computed P-wave velocity, v_p, versus wave frequency, f, as given by the pore-to-pore relaxation model for a model sandstone, at various levels of water saturation, S_w. These are the same data as plotted in Figure 3, but emphasize the velocity dispersion introduced by allowing for fluid pressure communication in the IBEMT.

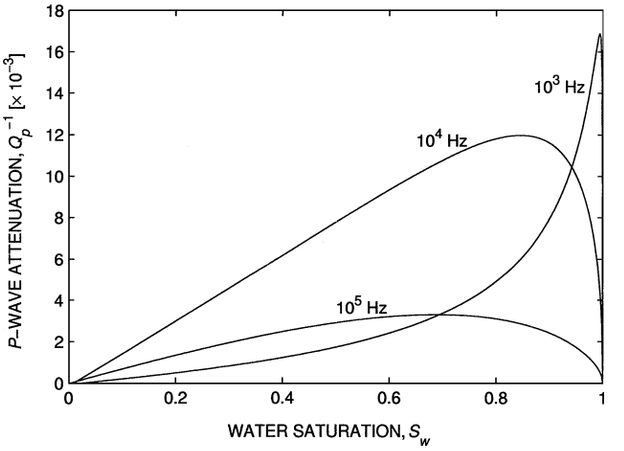

FIG. 5. Computed P-wave quality factor, Q_p^{-1}, versus water saturation, S_w, for a model sandstone, as given by the pore-to-pore relaxation model.

is decreased. This peak occurs at the saturation at which the distance over which a given water-filled inclusion must relax is such as to maximize the viscous loss over a wave cycle. As demonstrated in Figure 1, this occurs when the time scale of pressure relaxation is of the same order as the time scale of elastic deformation. The Q_p^{-1} versus S_w curves shown in Figure 5 are identical in form to the laboratory measurements shown in Figure 6 of Murphy et al. (1986), and are of the same order of magnitude.

Figure 6 shows Q_p^{-1} versus frequency at various levels of saturation. The behavior exhibited in this figure is typical of viscous relaxation phenomena. There is a broad attenuation peak centered about the relaxation frequency of the pore-to-pore relaxation mechanism, with attenuation tailing off to zero in the low- and high-frequency limits. Because the time scale of pressure relaxation increases with saturation (due to the fact that the pressures in individual water-filled inclusions must relax over greater distances to their nearest gas-filled inclusion), the attenuation peak shifts significantly toward lower frequencies with increasing saturation.

AN EXPLICIT PORE NETWORK MODEL

The principal failing of the pore-to-pore relaxation model developed in the previous section is the assumption that each inclusion is hydraulically connected to only one other inclusion, whereas real porous medium inclusions are multiply connected. Consequently, the model underestimates the permeability of the medium and the degree of pore-pressure relaxation that occurs at a given frequency. This limitation accounts for the discrepancy between the computed and low-frequency Gassmann predictions. An additional factor that cannot be accounted for is the role of pore-scale or sample-scale fluid distribution. Knight and Nolen-Hoeksema (1990) and Cadoret et al. (1995) provide experimental evidence for the stiffening effect of heterogeneous fluid distribution on elastic moduli. The simple pore-to-pore relaxation model does not provide a means of incorporating such effects into the relaxation dynamics.

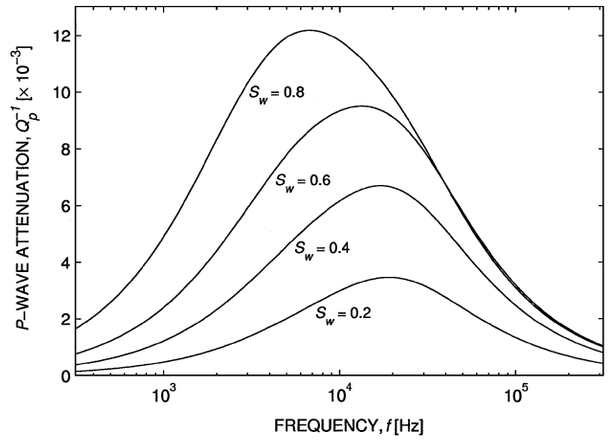

FIG. 6. Computed P-wave quality factor, Q_p^{-1}, versus wave frequency, f, as given by the pore-to-pore relaxation model for a model sandstone at various levels of water saturation, S_w. These are the same data as plotted in Figure 5, but emphasize the dispersion introduced by allowing for fluid pressure communication.

In order to model more accurately the frequency and saturation dependence of elastic wave velocities, we develop a relaxation model for a network of inclusions. In this system, each inclusion is hydraulically connected to any number of its neighboring inclusions, thus forming a hydraulically connected network. As in the previous model, we assume Poiseuille flow through the ducts in response to pressure gradients, such that the volumetric flow rate q_{ij} from inclusion i to inclusion j is given by

$$q_{ij} = \gamma_{ij}(p_i - p_j). \tag{10}$$

The fluid conductivity γ_{ij} $(i, j = 1, \ldots, n)$ is a function of the geometry of the duct, and for the case of a cylindrical duct is given by equation (2), under assumptions discussed in the previous section. In Appendix D, we derive the expression for the vector $\boldsymbol{\kappa}^*$ of effective moduli of every inclusion in the medium, under the simplifying assumption that all inclusions have the same shape. We obtain

$$\boldsymbol{\kappa}^* = \left(\mathbf{I} + \frac{1}{i\omega} \begin{bmatrix} \kappa_1/V_1 & 0 & \cdots \\ 0 & \kappa_2/V_2 & \cdots \\ \vdots & \vdots & \ddots \end{bmatrix} \mathbf{G} \right)^{-1} \boldsymbol{\kappa}, \tag{11}$$

where $\mathbf{I}$ is the identity matrix, the matrix $\mathbf{G}$ contains information about the hydraulic connections between pairs of inclusions, $\boldsymbol{\kappa}$ is the vector $(\kappa_1, \ldots, \kappa_n)$ of elastic moduli of fluids contained in the inclusions, and V_i is the volume of the ith inclusion.

Equation (11) merely generalizes equation (3) to the case of a multiply-connected pore space. In the high-frequency limit, it reduces to $\boldsymbol{\kappa}^* = \boldsymbol{\kappa}$, indicating as expected that communication between inclusions no longer plays a role at sufficiently high frequencies, and we recover the usual assumption of hydraulically isolated inclusions. As in the previous section, we use the expression $\mu^* = i\omega\eta$ for the effective shear modulus of fluid-filled inclusions to account for dissipation due to shear deformation of the fluid.

Modeling results and discussion

We compute effective bulk moduli and shear moduli for inclusions, as described above, and use Berryman's IBEMT to compute elastic wave velocities for the composite. We present in Figure 7 graphs of P-wave velocity, v_p, versus water saturation, S_w, at various frequencies for a model sandstone. The pore network was constructed by placing $n = 250$ spherical inclusions randomly within a solid sphere with the appropriate volume to generate a sample with the desired porosity, and placing a cylindrical duct between each inclusion and its three nearest neighboring inclusions (we assume that the ducts themselves contribute negligible porosity). The parameters describing the relevant dimensions and physical properties of the model sandstone are again as given in Tables 1 and 2. Saturation was varied by starting with all inclusions gas filled and randomly filling individual inclusions with water. Because the number of inclusions, n, in the conceptual sample is finite, the effects of increasing in saturation are discrete; hence the curves plotted in Figure 7 are not smooth. Increasing n smoothes the curves without significant quantitative change and at great computational cost [because of the matrix inversion in equation (11)].

We found $n = 250$ to be a satisfactory compromise between smoothness, accuracy, and computation time.

As expected, the high-frequency v_p versus S_w curve shown in Figure 7 reproduces the curve that would have been computed if an IBEMT without pore-pressure communication had been used. We also note that we obtain very close agreement with the Gassmann prediction in the low-frequency limit. However, the main improvement in this model over the simple pore-to-pore relaxation model is that the interconnectedness of the pore space is treated explicitly. Therefore, we expect that the details of the frequency dependence of v_p will be more realistic than that predicted with the previous model. Furthermore, this model is also suitable for investigating the effects of macroscopic fluid distribution, as explicit control is available over which inclusions are filled with which fluids.

In Figure 8 can be seen the details of the frequency-dependence of P-wave velocity for this model sandstone. This figure shows a graph of v_p versus frequency for the saturation level $S_w = 0.8$. For comparison, this figure also shows the corresponding curve from Figure 4. Figure 8 exhibits qualitative similarities with Figure 4, with the expected asymptotic limits for both high and low frequencies, and with a transition from low to high frequency occurring about a characteristic relaxation frequency, ω_0. [We see from equation (11) that a precise definition of ω_0 would be a complicated expression involving the matrix norm of **G**, but is on the order of the typical term $\gamma_{ij}\kappa_i / V_i$.] However, this figure differs substantially from Figure 4 in that the transition occurs over a much wider range of frequencies (over three decades of frequency rather than two) and is less symmetric about the central relaxation frequency.

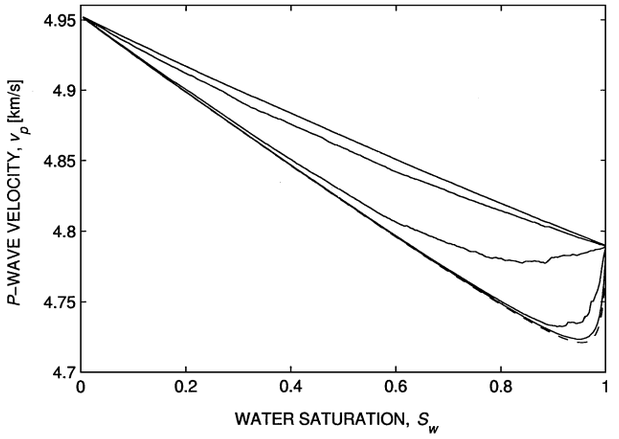

FIG. 7. Computed P-wave velocity, v_p, versus water saturation, S_w, for a model sandstone, as given by the pore-network relaxation model. The solid curves correspond to each of the wave frequencies 10^2, 10^3, 10^4, 10^5, and 10^6 Hz. For comparison, the velocities predicted by Gassmann's equation are plotted as the dashed curve.

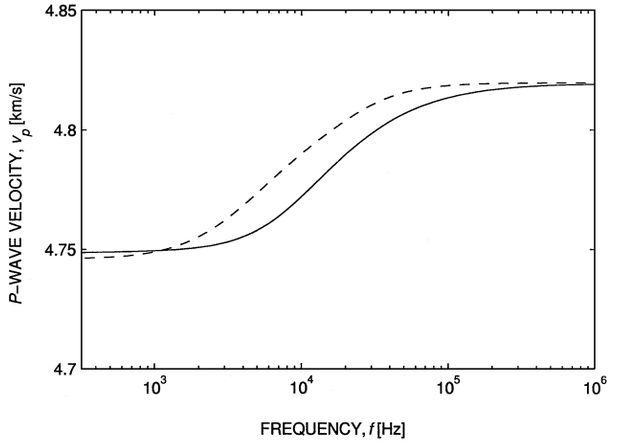

FIG. 8. Computed P-wave velocity, v_p, versus wave frequency, f, as given by the pore-network relaxation model for a model sandstone at 80% water saturation. The corresponding curve from Figure 4 is plotted as the dashed curve for comparison.

CONCLUSION

Our approach incorporates fluid relaxation into the constitutive elastic relations for individual inclusions. The response of a fluid-filled inclusion to sinusoidal deformation, including the effects of hydraulic connectivity of the pore space, is thereby represented entirely in the effective elastic moduli. To this end, we have developed explicit illustrative models of the relaxation process and used these models to derive frequency-dependent expressions for the effective moduli. The strength of this approach is that it lends itself to the development of more accurate models through the use of more sophisticated models of local flow (such was not our purpose here), without altering the proposed modeling framework.

For the models that we have considered, we have illustrated that our approach reproduces the previous inclusion-based velocity estimates in the high-frequency (unrelaxed) limit. More importantly, we have shown that in the low-frequency limit our results are consistent with (though not identical to) the Gassmann theory, where complete fluid pressure equilibration is assumed. In principle, equivalence with the Gassmann theory will be attained with a relaxation model that allows for equilibration of fluid pressures throughout the entire pore space at sufficiently low frequencies.

Of the two relaxation models we present, we consider the pore network model to be the most accurate and versatile. The effects of the random distribution of duct lengths, incorporated in an ad hoc manner into the pore-to-pore model, arise naturally in the construction of the inclusion network and need not be considered explicitly. The effects of long-range pore pressure communication are also accommodated, as illustrated by the correspondence of our velocity estimates with those of the Gassmann theory. Although not addressed in this study, the pore network model could be applied to systems in which the fluids are distributed in clusters or "patches" of inclusions.

While the pore network model is more general, it has the associated disadvantage that many pore-scale parameters must be supplied explicitly in any particular realization of the model. Another disadvantage of the network model is the increased computational cost associated with populating and inverting a large matrix. This is perhaps out of proportion with the degree of generality the model achieves. A related issue is that, owing to the complexity of the analytical results, they are less amenable to qualitative interpretation.

The inclusion-based models developed here retain the difficulty inherent in all effective medium theories: strong nonuniqueness in the prediction and interpretation of velocity

data. The number of model parameters (e.g., the geometry of inclusions and the parameters governing local flow) that are unknown makes it possible to reproduce any observed characteristic frequency and limiting velocities. The inverse problem of using our IBEMT approach to infer rock properties from measurements of velocity dispersion is therefore underdetermined. However, rather than a weakness of the effective medium approach, this reflects a fundamental difficulty that is due to the large number of variables on which elastic wave velocities depend. Although our introduction of local flow models into effective medium theory increases the problem of nonuniqueness by introducing extra free parameters, this is an unavoidable consequence of the tradeoff between the precision of the model and its accuracy in accounting for the relevant physics.

Inclusion-based effective medium theory is well-established as an effective means of modeling the physics associated with wave propagation in heterogeneous systems. By defining the elastic response of the inclusions in terms of complex moduli, we have shown that it is possible to incorporate relaxation mechanisms in the inclusion-based approach. With this modification IBEMT can be used to develop an improved understanding of the link between high-frequency and low frequency velocity measurements. This is a critical issue in determining how best to use the information obtained from laboratory studies in the interpretation of field seismic data.

ACKNOWLEDGMENTS

This research was supported by a Natural Sciences and Engineering Research Council of Canada Industrially-Oriented Research Grant to Rosemary Knight, with funding from Imperial Oil, Petro-Canada, and Western Atlas. Richard Taylor was also been supported in part by a University Graduate Fellowship from the University of British Columbia. We wish to thank Jack Dvorkin, two anonymous reviewers, and Associate Editor Ken Mahrer for their careful reviews of this manuscript and helpful comments.

REFERENCES

Berryman, J. G., 1980a, Long-wavelength propagation in composite elastic media. I. Spherical inclusions: J. Acoust. Soc. Am., **68**, 1809–1819.

——— 1980b, Long-wavelength propagation in composite elastic media. II. Ellipsoidal inclusions: J. Acoust. Soc. Am., **68**, 1820–1831.

Biot, M. A., 1956a, Theory of propagation of elastic waves in a fluid-saturated porous solid. I. Low frequency range: J. Acoust. Soc. Am., **28**, 168–178.

——— 1956b, Theory of propagation of elastic waves in a fluid-saturated porous solid. II. Higher-frequency range: J. Acoust. Soc. Am., **28**, 179–191.

Cadoret, T., Marion, D., and Zinszner, B., 1995, Influence of frequency and fluid distribution on elastic wave velocities in partially saturated limestones: J. Geophys. Res., **100**, 9789–9803.

Dutta, N. C., and Odé, H., 1979, Attenuation and dispersion of compressional waves in fluid-filled porous rocks with partial gas saturation (White model)—Part I: Biot theory; Part II: Results: Geophysics, **44**, 1777–1805.

Dvorkin, J., Nolen-Hoeksema, R., and Nur, A., 1994, The squirt-flow mechanism: Macroscopic description: Geophysics, **59**, 428–438.

Dvorkin, J., and Nur, A., 1993, Dynamic poroelasticity: A unified model with the squirt and the Biot mechanisms: Geophysics, **58**, 524–533.

Endres, A, 1998, Estimating the effects of pore geometry and pore fluid species on elastic wave velocity dispersion in rocks using microstructural models: Expl. Geophys., **29**, 361–367.

Endres, A. L., and Knight, R. J., 1997, Incorporating pore geometry and fluid pressure communication into modeling the elastic behavior of porous rocks: Geophysics, **62**, 106–117.

Gassmann, F., 1951, Über die elastizität at poröser medien: Vierteljahrsschrift der Naturforschenden Gesellschaft in Zürich, **96**, 1–23.

Jones, T. D., 1986, Pore fluids and frequency-dependent wave propagation in rocks: Geophysics, **51**, 1939–1953.

Knight, R., and Nolen-Hoeksema, R., 1990, A laboratory study of the dependence of elastic wave velocities on pore scale fluid distribution: Geophys. Res. Lett., **17**, 1529–1532.

Kuster, G. T., and Toksöz, M. N., 1974, Velocity and attenuation of seismic waves in two-phase media: Part I. Theoretical formulations: Geophysics, **39**, 587–606.

le Ravalec, M., Guéguen, Y., and Chelidze, T., 1996, Elastic wave velocities in partially saturated rocks: Saturation hysteresis: J. Geophys. Res., **101**, B1, 837–844.

Mavko, G., Mukerji, T., and Dvorkin, J., 1998, The rock physics handbook: Cambridge University Press.

Murphy, W. F., Winkler, K. W., and Kleinberg, R. L., 1986, Acoustic relaxation in sedimentary rocks: Dependence on grain contacts and fluid saturation: Geophysics, **51**, 757–766.

White, F. M., 1986, Fluid mechanics, 2nd ed.: McGraw-Hill.

Xu, S., 1998, Modelling the effect of fluid communication on velocities in anisotropic porous rocks: Internat. J. Solids and Structures, **35**, 4685–4707.

APPENDIX A

EFFECTIVE BULK MODULUS FOR PORE-TO-PORE RELAXATION

We consider two fluid-filled inclusions, with volumes V_1 and V_2, filled with fluids having bulk moduli κ_1 and κ_2, respectively. We take the inclusions to be imbedded in an infinite background medium subjected to an externally applied incremental dilatation $d\theta^A$ at infinity. The following result derived by Endres and Knight (1997),

$$d\theta_i + \frac{dp_i}{\kappa_b} = \left(d\theta^A + \frac{dp_i}{\kappa_b}\right) P(\kappa_b, \mu_b, \kappa_i, \mu_i, \alpha), \quad \text{(A-1)}$$

relates the incremental dilatation $d\theta^i$ of inclusion i to $d\theta^A$ and the incremental change in fluid pressure dp_i in the inclusion ($i = 1, 2$). The terms κ_b, μ_b are the bulk and shear moduli of the background medium, respectively. The quantities $P(\kappa_b, \mu_b, \kappa_i, \mu_i, \alpha) \equiv P_i$ are identical to the P^{*i} defined in Berryman (1980b), and account for the effects of inclusion geometry via the aspect ratio α. We take the shear moduli μ_i of the fluids to be zero.

If q is the instantaneous volumetric flow rate of fluid from inclusion 1 to inclusion 2, then the pressure increments dp_i in the fluids are given by the following relations,

$$dp_1 = -\kappa_1\left(d\theta_1 + \frac{q}{V_1}dt\right)$$
$$dp_2 = -\kappa_2\left(d\theta_2 - \frac{q}{V_2}dt\right), \quad \text{(A-2)}$$

which follow directly from the constitutive elastic relations for the fluids. We assume that q can be written in the form

$$q = \gamma(p_1 - p_2), \quad \text{(A-3)}$$

where γ is the fluid conductivity between the inclusions.

Assuming a time dependence of the form $e^{i\omega t}$ for the quantities θ^A, θ_1, θ_2, p_1, and p_2, equations (A-1)–(A-3) can be combined to relate the fluid pressure p_1 in inclusion 1 to its

dilatation θ_1. This yields an expression of the form

$$p_1 = -\kappa^* \theta_1, \tag{A-4}$$

which defines the effective bulk modulus κ_1^* of the inclusion material. We obtain

$$\kappa_1^* = \frac{\tilde{\kappa} + i\dfrac{\omega}{\omega_0}\kappa_1}{1 + i\dfrac{\omega}{\omega_0}}, \tag{A-5}$$

where $\tilde{\kappa}$ is given by

$$\tilde{\kappa} = \frac{P_1 V_1 + P_2 V_2}{P_1\left(\dfrac{V_1}{\kappa_1} + \dfrac{V_2}{\kappa_2}\right) + \dfrac{V_2}{\kappa_b}(P_2 - P_1)}, \tag{A-6}$$

and the characteristic frequency ω_0 is given by

$$\omega_0 = \frac{\gamma}{V_1 V_2}\left[\frac{\kappa_1 \kappa_2}{\kappa_b - \kappa_2 + P_2 \kappa_2}\right] \times \left[\kappa_b\left(\frac{V_1}{\kappa_1} + \frac{V_2}{\kappa_2}\right) + V_2\left(\frac{P_2}{P_1} - 1\right)\right], \tag{A-7}$$

APPENDIX B

EFFECTIVE BULK MODULI FOR INCLUSIONS WITH IDENTICAL GEOMETRY

If we make the simplifying assumption that $P_1 = P_2$ (i.e., if both inclusions have the same shape), we can rewrite equations (A-6) and (A-7) in the form

$$\frac{1}{\tilde{\kappa}} = \frac{V_1/(V_1 + V_2)}{\kappa_1} + \frac{V_2/(V_1 + V_2)}{\kappa_2}, \tag{B-1}$$

$$\omega_0 = \gamma \frac{\dfrac{\kappa_1}{V_1} + \dfrac{\kappa_2}{V_2}}{1 + \dfrac{\kappa_2}{\kappa_b}(P_1 - 1)}. \tag{B-2}$$

In this case, we see that the low-frequency limit $\tilde{\kappa}$ of κ_1^* is just the volumetric Reuss average of the bulk moduli κ_1 and κ_2. This is the expected behavior when the fluid pressures are equal in both inclusions (i.e., complete pressure communication). Since we consider fluid-filled inclusions in a solid matrix, we assume that $\kappa_2 \ll \kappa_b$, so that to a good approximation we can write equation (B-2) as

$$\omega_0 \approx \gamma\left(\frac{\kappa_1}{V_1} + \frac{\kappa_2}{V_2}\right). \tag{B-3}$$

Note that equations (B-1) and (B-3) are exactly what would have been obtained if we had assumed in Appendix A that $\theta_1 = \theta_2$ and used only equations (A-2) and (A-3) to derive the expression for κ_1^*. This observation is used as a simplifying assumption in our development of the pore network model.

APPENDIX C

PROBABILITY DISTRIBUTION OF DISTANCES BETWEEN INCLUSIONS

Let Ω denote an arbitrary region of volume V in a porous medium. Let N points (the centers of inclusions) be chosen randomly with uniform distribution over Ω, and define the random variable r to be the distance from a given point $\mathbf{x}_0$ in Ω to the nearest of these points. Denote by Ω_0 the sphere of radius R and volume $V_0(R)$ centered at $\mathbf{x}_0$.

Defining the distribution function $F(R) \equiv \wp(r \le R) =$ "the probability that $r \le R$", we then have

$$\begin{aligned} F(R) &= \wp\,(\text{there is at least one point in } \Omega_0) \\ &= 1 - \wp\,(\text{all } N \text{ points are outside } \Omega_0) \\ &= 1 - \left(\frac{V - V_0(R)}{V}\right)^N. \end{aligned} \tag{C-1}$$

Defining $n \equiv N/V$ (the number density of inclusions), we can write

$$F(R) = 1 - \left(1 - \frac{n V_0(R)}{N}\right)^N. \tag{C-2}$$

We are interested in the limiting case where the size of Ω is much greater than the typical distance r, so we let $N \to \infty$ and $V \to \infty$ in equation (C-2) with n held fixed to yield

$$F(R) = 1 - \exp(-n V_0(R)) = 1 - \exp\left(\tfrac{4}{3}\pi n R^3\right). \tag{C-3}$$

Denoting the density of r by $P(R)$, so that $F(R) = \int_0^R P(s)ds$, we then arrive at

$$P(R) = F'(R) = 4\pi n R^2 \exp\left(\tfrac{4}{3}\pi n R^3\right) \tag{C-4}$$

APPENDIX D

EFFECTIVE BULK MODULI FOR PORE THE NETWORK MODEL

Here, we consider effective bulk moduli for a network of N fluid-filled inclusions, allowing each inclusion to have fluid pressure communication with any number of its neighboring inclusions. To simplify our development, we assume that all inclusions have the same shape, so that by our observation in Appendix B we can assume that all inclusions undergo the same volumetric dilatation θ (this assumption is easily relaxed, at some expense in complexity of notation).

If q_{ij} is the instantaneous volumetric flow rate from inclusion i to inclusion j, then the differential equations analogous to equation (A-2) are

$$\frac{dp_i}{dt} = -\kappa_i\left(\frac{d\theta}{dt} + \frac{q_{im} + q_{in} + \cdots}{V_i}\right), \tag{D-1}$$

$i = 1, 2, \ldots, N$, where $m, n, \ldots$ are the indices of the inclusions to which inclusion i is hydraulically connected, κ_i is the bulk

modulus of the fluid in the inclusion, and V_i is the inclusion's volume. Again we assume that the q_{ij} can be written in the form

$$q_{ij} = \gamma_{ij}(p_i - p_j), \tag{D-2}$$

where γ_{ij} is the hydraulic conductivity between inclusion i and inclusion j (inclusions that are not directly connected have $\gamma_{ij} = 0$; we take $\gamma_{ii} = 0$ for all i). Assuming a time dependence of the form $e^{i\omega t}$ for the quantities $p_i, p_j, \ldots$ and θ, we can rewrite equation (D-1) as

$$i\omega p_i = -i\omega\kappa_i\theta - \frac{\kappa_i}{V_i}\sum_{j=1}^{N}\gamma_{ij}(pi - p_j). \tag{D-3}$$

To simplify our notation, we define quantities γ_i^* by

$$\gamma_i^* = \sum_{j=1}^{N}\gamma_{ij}, \tag{D-4}$$

and the matrix $\mathbf{G}$ by

$$\mathbf{G} = \begin{bmatrix} \gamma_1^* & -\gamma_{12} & \cdots & -\gamma_{iN} \\ -\gamma_{21} & \gamma_2^* & \cdots & -\gamma_{2N} \\ \cdots & \cdots & \cdots & \cdots \\ \gamma_{N1} & -\gamma_{N2} & \cdots & \gamma_N^* \end{bmatrix}. \tag{D-5}$$

(Note that $\mathbf{G}$ is a symmetric matrix, since $\gamma_{ij} = \gamma_{ji}$.) Defining vectors of pore pressures and pore fluid bulk moduli by

$$\mathbf{P} = \begin{bmatrix} p_1 \\ p_2 \\ \vdots \end{bmatrix}, \quad \text{and} \quad \boldsymbol{\kappa} = \begin{bmatrix} \kappa_1 \\ \kappa_2 \\ \vdots \end{bmatrix}, \tag{D-6}$$

we can write equations (D-3) as

$$i\omega\mathbf{p} = -i\omega\boldsymbol{\kappa}\theta - \begin{bmatrix} \kappa_1/V_1 & 0 & \cdots \\ 0 & \kappa_2/V_2 & \cdots \\ \vdots & \vdots & \ddots \end{bmatrix}\mathbf{G_p}. \tag{D-7}$$

We can then rewrite equation (D-7) in the form

$$\mathbf{p} = -\boldsymbol{\kappa}^*\boldsymbol{\theta}, \tag{D-8}$$

which defines the vector of effective bulk moduli $\boldsymbol{\kappa}^*$ for the inclusion materials in all N inclusions. Thus we obtain

$$\boldsymbol{\kappa}^* = \left(\mathbf{I} + \frac{1}{i\omega}\begin{bmatrix} \kappa_1/V_1 & 0 & \cdots \\ 0 & \kappa_2/V_2 & \cdots \\ \vdots & \vdots & \ddots \end{bmatrix}\mathbf{G}\right)^{-1}\boldsymbol{\kappa}, \tag{D-9}$$

where $\mathbf{I}$ is the $N \times N$ identity matrix.